Analysis of Shock Motion in STBLI Induced by a Compression Ramp Configuration Using DNS Data

M. Wu*and M.P. Martin†

Mechanical and Aerospace Engineering Department

Princeton University, Princeton, NJ 08540

DNS data of a 24° compression ramp configuration are used to analyze the shock motion. The motion of the shock is evident visually in an animation generated from the DNS data. Wall-pressure and mass-flux signals measured in the free stream also indicate that there is shock motion. Wu & Martin[1] showed that the motion of the shock has a characteristic low frequency with a range of 0.007-0.013 U_∞/δ (0.7-1.2 kHz). The shock motion exhibits spanwise wrinkling and streamwise oscillation. The spanwise wrinkling is mainly caused by the spanwise nonuniformity of turbulent structures in the incoming boundary layer. A correlation is found between the spanwise wrinkling motion of the shock and the mass flux in the incoming boundary layer. In studying the streamwise motion of the shock, statistics for the incoming boundary layer are gathered conditionally based on the location of the shock. The results show that there is insignificant difference in the mean velocity profile when the shock location is upstream or downstream of the mean location. In contrast, significant difference is found in the Reynolds stress. Moreover, a correlation is found between the Reynolds stress signal in the incoming boundary layer and the streamwise shock location.

Nomenclature

M	Freestream Mach number
δ	Thickness of the incoming Boundary layer
δ^*	Displacement thickness of the incoming Boundary layer
δ^+	Displacement thickness of the incoming Boundary layer in wall units
θ	Momentum thickness of the incoming Boundary layer
Re_θ	Reynolds number based on θ
C_f	Skin friction coefficient
x	Coordinate in the streamwise direction
y	Coordinate in the spanwise direction
z	Coordinate in the wall-normal direction
Subscript	
∞	Freestream value
w	value at the wall

*Graduate Student, Student Member AIAA.

†Assistant Professor, Member AIAA.

I. Introduction

Shockwave/turbulent boundary layer interaction (STBLI) is a complex problem with great practical importance. Physical understanding of the problem is the essence of efficient design of scram-jet engines and hypersonic vehicles. However, many aspects of the problem such as dynamics of shock unsteadiness, turbulent amplification, separation and reattachment criteria, and unsteady heat transfer near the separation and reattachment points, are still not fully understood.

The compression ramp configuration is one of the canonical configurations that have been studied extensively in experiments since 1970's. One of the outstanding issues in STBLI is that the shock motion has a frequency much lower than the characteristic frequency of the incoming boundary layer. The time scale of the low frequency motion is $O(10\delta/U_\infty)$ as reported from various experiments[2–4] while the characteristic time scale of the incoming boundary layer is $O(\delta/U_\infty)$. The cause of this low frequency motion is still a debating issue. Andreopoulos & Muck[5] concluded that the shock motion is driven by the bursting events in the incoming boundary layer. Recently, Ganapathisubramani et al.[6] proposed that very long coherent structures or superstructures in the incoming boundary layer are responsible for the low frequency motion of the shock. The length of these structures can be $O(10\delta)$ or even longer. Ringuette, Wu & Martin[7] analyzed structures in supersonic boundary layers using DNS data and confirmed the existence of such long coherent structures in the DNS.

In spite of the fact that superstructures are found in our DNS data, we are yet unable to correlate these structures with the shock motion using current DNS data analyses. It should be pointed out that if the superstructures are causing the low frequency shock motion, then the low frequency motion must be the spanwise wrinkling shock motion. This is because high and low speed superstructures alternate in the spanwise direction with a distance of $0.5 - 1\delta$. However, our DNS data show that the low frequency motion is a global streamwise direction motion of the shock in the whole spanwise direction of the computational domain. The spanwise wrinkling is a local motion embedded in the streamwise direction motion.

In this paper, the simulation conditions are given in Section II. The spanwise and streamwise shock motion are studied in Section III(A) and Section III(B), respectively. Finally, conclusions are presented in Section IV.

II. Simulation Conditions

M	Re_θ	θ (mm)	δ^* (mm)	δ (mm)	δ^+	C_f
2.9	2300	0.38	1.80	6.4	320	0.0021

Table 1. Flow conditions for the DNS.

The flow configuration is a 24° compression ramp. Figure 1 plots the computational domain for the DNS. The number of grid points is $1024 \times 160 \times 128$ in the streamwise, spanwise, and wall-normal directions, respectively. The inflow conditions for the DNS are shown in Table II. Notice that the Reynolds number is relatively lower than that of most existing experiments for the same configuration. Details about the DNS can be found in Wu & Martin.[1,8]

III. Shock motion

Figure 2(a) plots three wall-pressure signals measured at different streamwise locations upstream of the ramp corner (the corner is located at $x = 0$) along the spanwise center line of the computational domain. For the signal measured in the incoming boundary layer at $x = -6.9\delta$, the magnitude normalized by P_∞ is around one with small fluctuations. For the signal at $x = -2.98\delta$, which is the mean separation point (defined as the point where the mean skin friction coefficient changes sign from positive to negative), the magnitude fluctuates between 1 to 1.2. For the signal measured at $x = -2.18\delta$, the magnitude oscillates between 1.5 and 2. The energy spectra of these three signals are plotted in Figure 2(b). To avoid overlapping, the spectra for the signals at $x = -2.98\delta$ and $x = -2.18\delta$ are multiplied by 10^3 and 10^6, respectively. One can see that for the signals measured at the mean separation point and inside the separation bubble, the peak is at a much lower frequency ($f = 0.007 - 0.01U_\infty/\delta$) than that of the signal measured in the incoming boundary layer.

Figure 3 plots iso-surfaces of magnitude of gradient of pressure showing the shock structure at two instants. In Figure 3(a), the shock is at its most upstream location. While in Figure 3(b) the shock is at its most downstream location. There is a displacement of the shock location in the streamwise direction. Another phenomenon to notice is that near the shock foot region, the shock wrinkles in the spanwise direction. However, further away from the shock foot, the shock is quite flat in the spanwise direction.

To show the different characteristics of the shock motion at different wall-normal locations, contours of the magnitude of the gradient of pressure on streamwise-spanwise planes are plotted in Figure 4. Two instantaneous flow fields are plotted at distances of 0.9δ and 2δ away from the wall. In Figures 4(a) and (b), the shock is nearly uniform in the spanwise direction, as we have seen in Figure 3. Also the movement of the shock is evident. Figures 4(c) and (d) plot the same instants at a plane closer to the wall. Here we observe a clear wrinkling of the shock in the spanwise direction. The shock also moves in the streamwise direction in the same manner as shown in Figures 4(a) and (b). Moreover, the scale of the motion in the streamwise direction is greater than that of the spanwise wrinkling, which will be presented in detail in the following sub-sections.

Thus, the shock motion contains two aspects. One is that the shock wrinkles along the spanwise direction near the shock foot region. The other corresponds to the shock moving upstream and downstream in the streamwise direction. The motion that is inferred from the wall-pressure signal in Figure 2 results from the combination of these two aspects. However, the low frequency motion is actually related to the motion in the streamwise direction rather than to the spanwise wrinkling. This can be seen by looking at mass-flux signals measured in the free stream as shown in Figure 5. Here the mass-flux signals are measured at different streamwise locations (upstream, inside, and downstream of the shock motion region) with a distance of 2δ away from the wall. The choice of the spanwise location does not make significant difference because at this distance away from the wall, the shock is uniform in the spanwise direction. In Figure 5(a), the mass-flux signal measured inside the shock motion region oscillates between those measured upstream and downstream of the shock motion region, indicating that the shock is moving upstream and downstream of that point. The energy spectra plotted in Figure 5(b) show that the characteristic low frequency range is between $0.007 - 0.013U_\infty/\delta$, which is roughly the same as that given by the wall-pressure signals in Figure 2(b).

A. Spanwise wrinkling shock motion

Figure 6 plots normalized iso-surfaces of $|\nabla\rho|$ for four consecutive instantaneous flow fields. The structures in the incoming boundary layer and the shock are seen. Two structures are highlighted in Figures 6(a) and 6(c). For an adiabatic wall, these structures contain low momentum fluid. The wall is set to be isothermal in the DNS. However, the temperature is very close to the adiabatic wall temperature. Thus, these structures convect while uplifting low density and low speed fluid from the wall. As these two structures pass through the shock, the shock curves toward the upstream, resulting in spanwise wrinkling of the shock as shown in

Figures 4(c) and (d).

To show a more quantitative relationship between the spanwise wrinkling of the shock and the structures in the incoming boundary, the correlation between the pressure at the spanwise-mean shock location and the mass flux in the incoming boundary layer at a distance of 0.7δ away from the wall is plotted in Figure 7(a). The reason to choose $z = 0.7\delta$ is that at this location the shock is not diffused too much in the DNS so that shock location can be well defined. The mass flux is measured at a location 5δ upstream of the ramp corner. The instantaneous shock location is defined as the point at which the pressure rises to $1.3P_\infty$ in the streamwise direction. The spanwise-mean shock location is computed by spanwise averaging at each instant. In other words, the spanwise-mean shock location is a function of time. A peak of the correlation if observed at $\tau = -3.3\delta/U_\infty$ with a magnitude of about 0.35. Figure 7(b) plots the "enhanced" correlation, which is enhanced in that the contribution to the correlation is only computed whenever the difference between the instantaneous shock location and the spanwise-mean location is greater than 0.15δ (or 1.5 standard deviation of the spanwise wrinkling shock location). In other words, only strong events are accounted for. The enhanced correlation has similar shape with the correlation shown in Figure 7(a). It peaks at the same location with a much greater magnitude. The similar characteristics observed in Figures 7(a) and 7(b) indicate that the correlation is mainly influenced by strong events such as those observed in Figure 6.

B. Streamwise shock motion

The same correlation between pressure and mass flux is also computed using a different definition of the mean shock location. Here the mean shock location is computed by spanwise and temporal averaging. Thus, it is a fixed point and does not vary with time. The correlation and enhanced correlation are plotted in Figure 8. In Figure 8(a), a peak is observed at the same location as in Figure 7(a), but with a much smaller magnitude. The same criterion as that in the previous sub-section is used to compute the enhanced correlation. i.e., the correlation is computed only when the instantaneous shock location deviates from the mean more than 0.3δ, which is 1.5 standard deviation of the streamwise shock location. Again, the enhanced correlation peaks at the same location with a greater magnitude. However, the peak magnitude observed in Figure 8(b) is much smaller than that in Figure 7(b). Thus, the streamwise shock motion is not mainly affected by low momentum structures in the incoming boundary layer.

As discussed in the beginning of the section, low frequency shock motion is related to the streamwise direction shock motion in the DNS. The streamwise shock motion is observed as the shock moves upstream and downstream globally in the entire spanwise direction of the computational domain. No matter what form of motion it is, something happening in the incoming boundary layer is believed to drive the shock motion. To study the difference in the incoming boundary as the shock moves upstream and downstream, conditional statistics are calculated. Statistics are gathered in a 4δ region of the inlet, where streamwise and spanwise averaging is performed whenever the shock is located at a distance greater than 1.5σ upstream/downstream of the mean location, where σ is the standard deviation of the shock location. The shock location is measured at 2δ away from the wall. Again, the mean shock location is computed by spatial and temporal averaging. The instantaneous shock location is averaged in the spanwise direction at each instant, i.e., there is only one shock location at each instant. The conditional properties of the incoming boundary layer are shown in Table 2. No significant difference is found in these properties. Figure 9 plots the mean velocity profiles conditioned on the shock location. The profile is a little fuller when the shock is at a downstream location. However, the difference is very small (less than 3%).

Figure 10 plots the conditionally averaged Reynolds stress profiles. In the near wall region ($z < 0.2\delta$), no difference is observed. In contrast, in a region of $0.2 < z/\delta < 0.8$, there is a significant difference. When the shock is at a upstream location, the Reynolds stress is up to 35% higher than that when the shock is at a downstream location. We suspect that the change of Reynolds stress is the cause of the low frequency shock motion. To verify this, two signals are plotted in Figure 11. The mass-flux signal (averaged in the spanwise direction) measured inside the shock motion region in the free stream ($z = 2\delta$) indicates when the shock is

Shock location	δ (mm)	θ (mm)	δ^* (mm)	C_f
Upstream	6.3	0.379	1.71	0.00215
Downstream	6.5	0.374	1.76	0.00219

Table 2. Conditional properties of the incoming boundary layer based on the shock location.

upstream or downstream of that location. The Reynolds stress signal is measured in the incoming boundary layer and averaged in a 4δ region in the streamwise direction as well as in the spanwise direction. A clear correlation is seen between these two signals. The correlation coefficient is about 0.4. Figure 12 plots the energy spectra of these two signals. Both spectra are normalized by their maximum value. Again we see that the two signals peak at the same frequency of roughly $0.013U_\infty/\delta$ (1.2 kHz).

IV. Conclusion

Low frequency motion is evident in the DNS of a 24° compression ramp. The characteristic frequency of the shock motion is about $0.013U_\infty/\delta$. While experiments are typically confined to 2-dimensional view of the shock motion, DNS data provides a way to study the shock motion in 3-dimensional space. Our analysis shows that the motion is characterized by a large scale streamwise motion and a relative smaller scale spanwise wrinkling. The low frequency motion is mainly influenced by the streamwise motion. While the spanwise wrinkling is a local feature. Mass flux in the incoming boundary layer is related to the spanwise wrinkling motion, indicating that this motion may be related to bursting events in the incoming boundary layer. Conditional statistics of the incoming boundary layer are calculated based on the instantaneous spanwise-averaged streamwise shock location. No significant difference is found in the mean velocity profile. However, significant difference is found in the Reynolds stress. Moreover, a correlation is found between the location of the shock and the Reynolds stress in the incoming boundary layer.

Acknowledgments

This work is supported by the Air Force Office of Scientific Research under grant AF/F49620-02-1-0361.

References

[1] Wu, M. and Martin, M. P., "Direct Numerical Simulation of Shockwave and Turbulent Boundary Layer Interaction induced by a Compression Ramp," *submitted to AIAA Journal*, 2006.

[2] Dolling, D. S. and Or, C. T., "Unsteadiness of the Shock Wave Structure in Attached and Separated Compression Ramp Flows," *Experiments in Fluids*, Vol. 3, No. 1, 1985, pp. 24–32.

[3] Selig, M. S., *Unsteadiness of Shock Wave/Turbulent Boundary Layer Interactions with Dynamic Control*, Ph.D. thesis, Princeton University, 1988.

[4] Dussauge, J. P., Dupont, P., and Devieve, J. F., "Unsteadiness in Shock Wave Boundary Layer Interactions with Separation," *Aerospace Science and Technology*, Vol. 10, No. 2, 2006.

[5] Andreopoulos, J. and Muck, K. C., "Some New Aspects of The Shock-wave/Boundary-layer Interaction in Compression-ramp Flows," *Journal of Fluid Mechanics*, Vol. 180, July 1987, pp. 405–428.

[6] Ganapathisubramani, B., Clemens, N. T., and Dolling, D. S., "Planar Imaging Measurements to Study The Effect of Spanwise Structure of Upstream Turbulent Boundary Layer on Shock Induced Separation," *AIAA Paper No. 2006-324*, Jan. 2006.

[7] Ringuette, M. J., Wu, M., and Martin, M. P., "Coherent Structures in DNS of Supersonic Turbulent Boundary Layers at Mach 3," *AIAA Paper No. 2007-1138*, 2007.

[8]Wu, M. and Martin, M. P., "New DNS Results of Shockwave/Turbulent Boundary Layer Interaction," *AIAA Paper No. 2006-3037*, Jun. 2006.

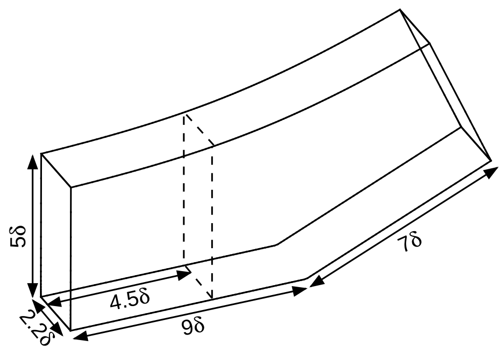

Figure 1. Computational domain of the DNS.

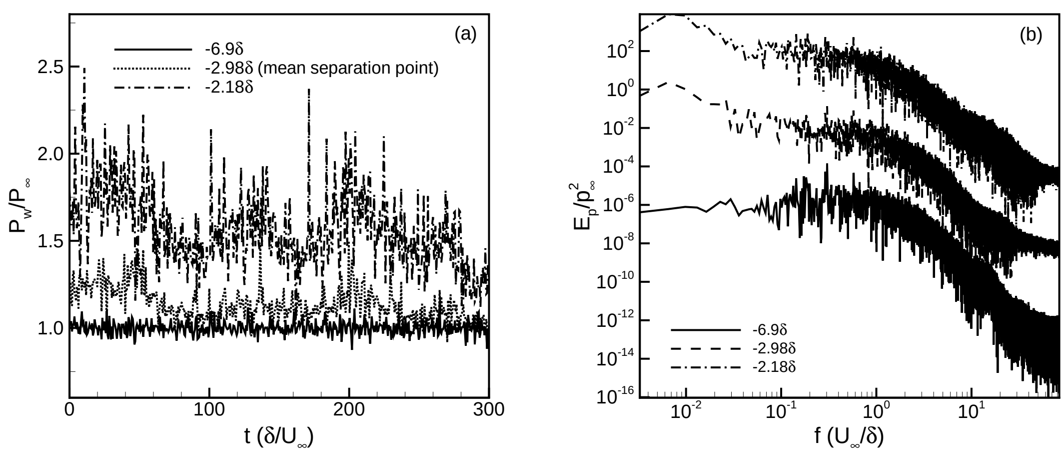

Figure 2. Wall-pressure signals (a) and corresponding energy spectra (b) at different streamwise locations relative to the ramp location.

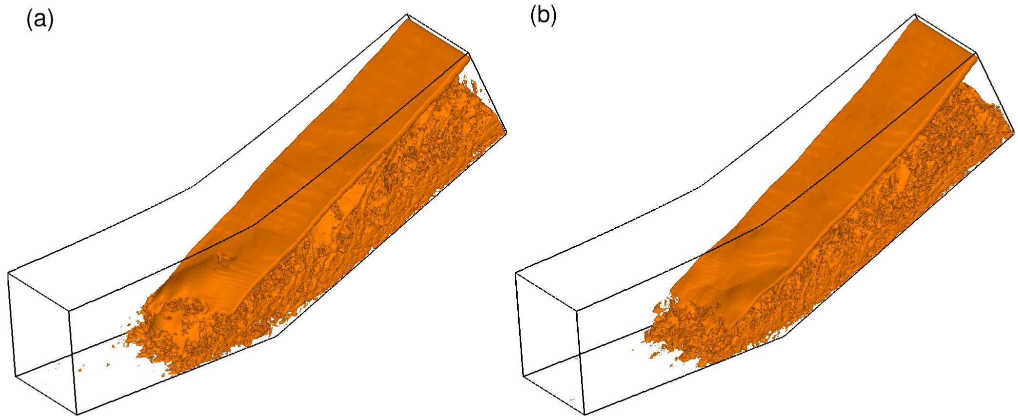

Figure 3. $|\nabla p| = 0.5P_\infty/\delta$ **showing the most upstream (a) and downstream (b) shock position.**

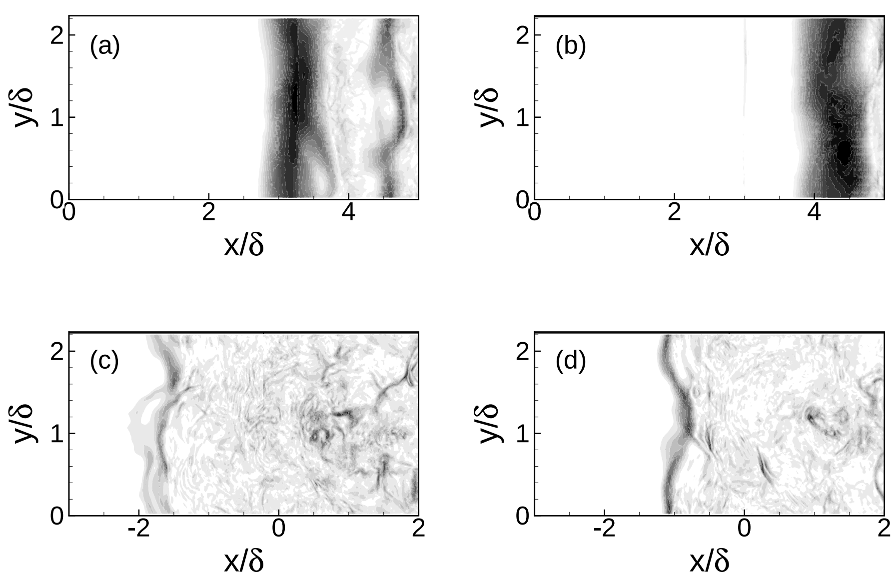

Figure 4. Contours of $|\nabla p|$ **showing the shock location for two instants at** $z = 2\delta$ **((a) & (b)) and the same instants at** $z = 0.9\delta$ **((c) & (d)).**

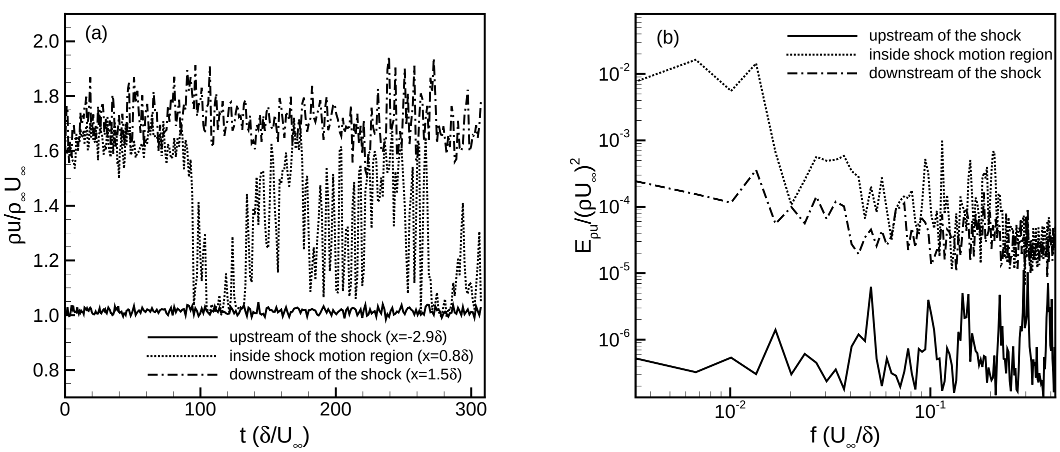

Figure 5. (a) Mass-flux signals and (b) corresponding energy spectra measured at different streamwise location at $z = 2\delta$.

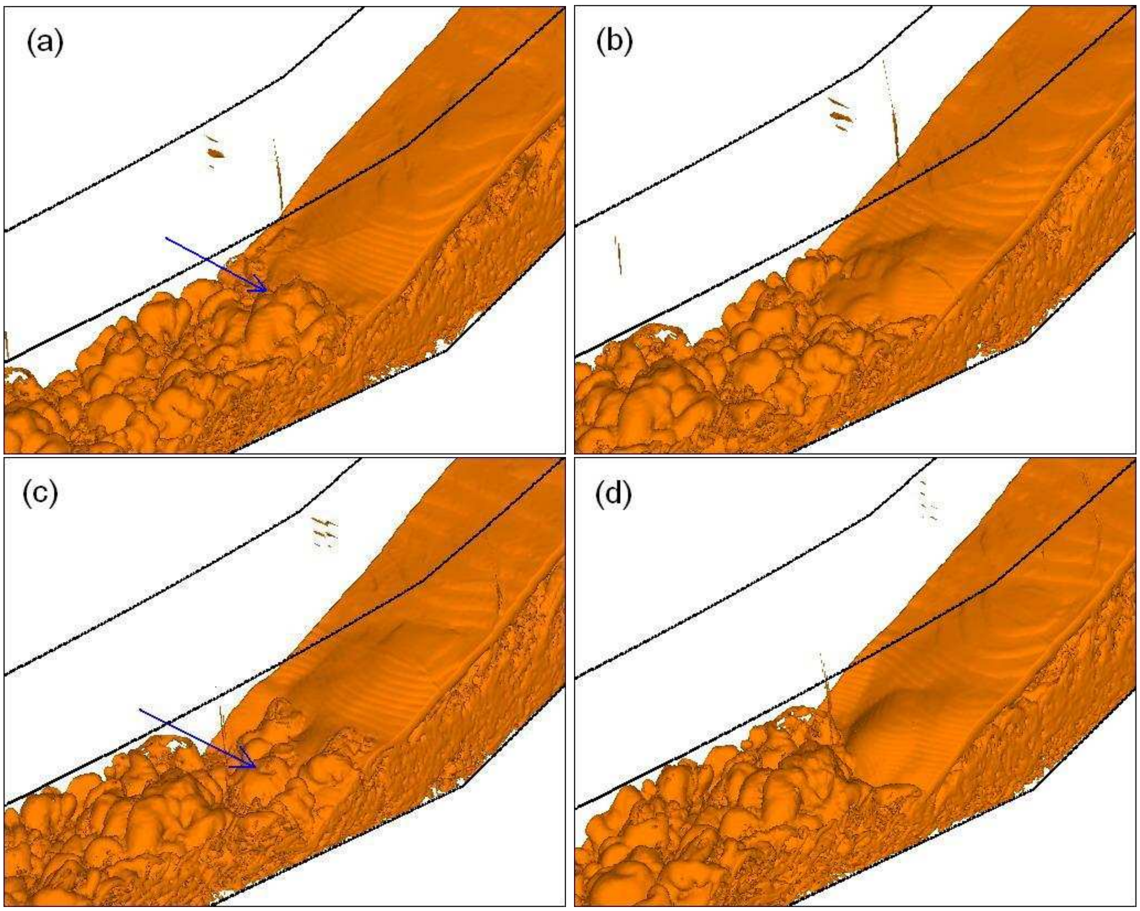

Figure 6. Iso-surface of $|\nabla\rho| = 2\rho_\infty/\delta$ showing structures in the incoming boundary layer passing through the shock.

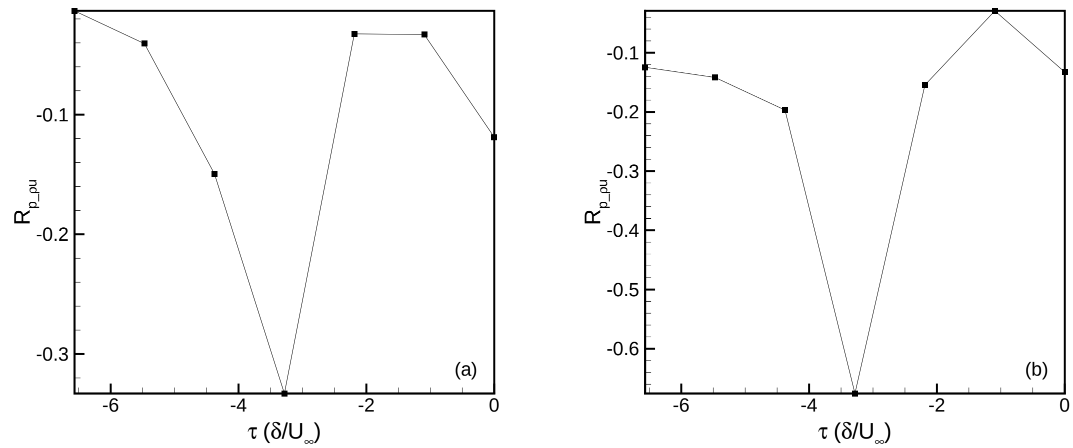

Figure 7. Correlation (a) and enhanced correlation (b) between mass flux at $x = -5\delta$ and pressure at the instantaneous spanwise-mean shock location at $z = 0.7\delta$.

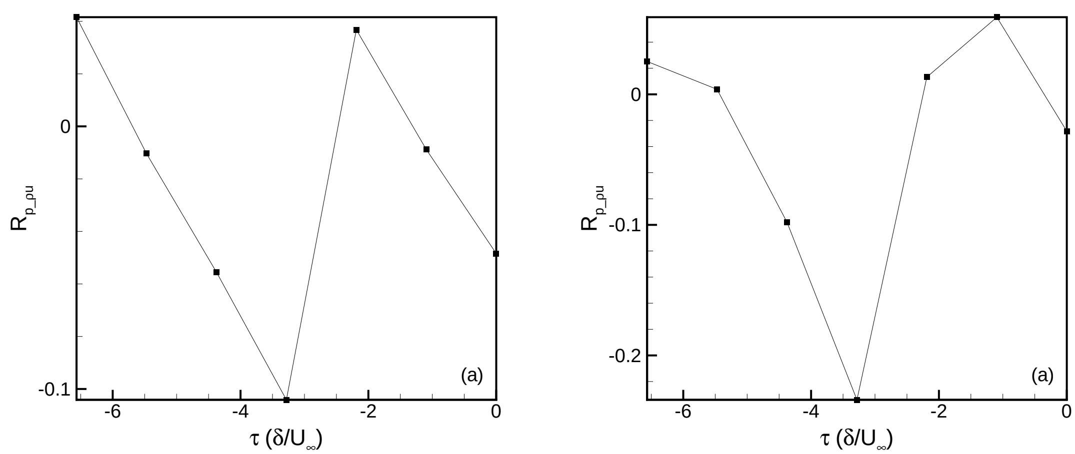

Figure 8. Correlation (a) and enhanced correlation (b) between mass flux at $x = -5\delta$ and pressure at the mean shock location at $z = 0.7\delta$.

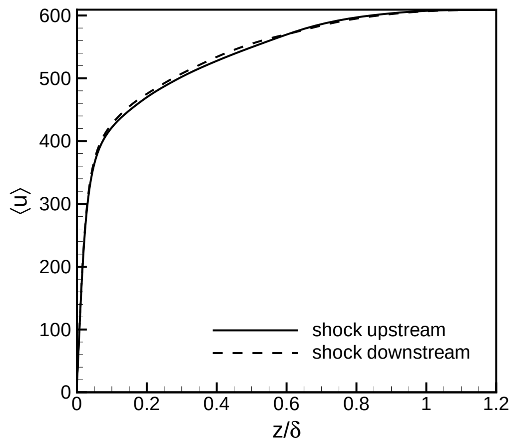

Figure 9. Comparison of the conditionally averaged mean velocity profile for the incoming boundary layer.

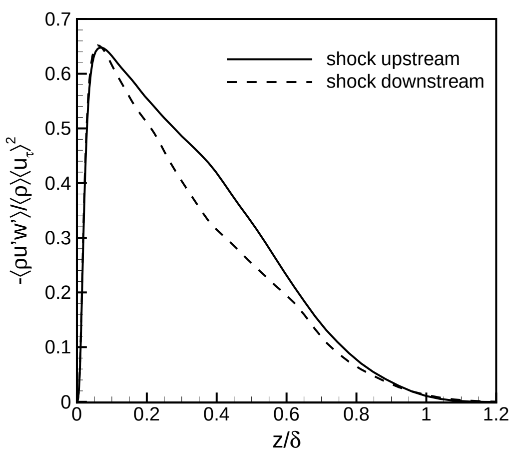

Figure 10. Comparison of the conditionally averaged Reynolds stress component $\rho u'w'$ for the incoming boundary layer.

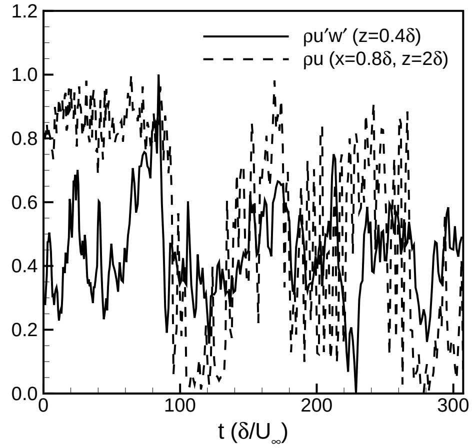

Figure 11. Mass-flux signal measured in the free stream and $\rho u'w'$ signal measured inside the incoming boundary layer showing a correlation.

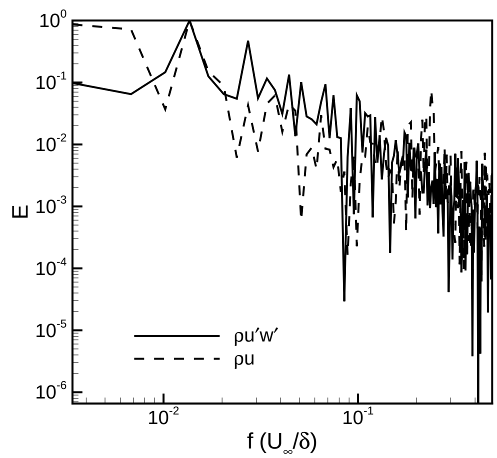

Figure 12. Energy spectra of the mass-flux signal measured in the free stream and $\rho u'w'$ signal measured inside the incoming boundary layer.